

# Interferometric optical fiber sensor for optoacoustic endomicroscopy

Okan Ülgen<sup>1,2</sup>  | Rami Shnaiderman<sup>1,2</sup> | Christian Zakian<sup>1,2</sup> | Vasilis Ntziachristos<sup>1,2\*</sup>

<sup>1</sup>Chair of Biological Imaging at the Central Institute for Translational Cancer Research (TranslaTUM), School of Medicine, Technical University of Munich, Munich, Germany

<sup>2</sup>Institute of Biological and Medical Imaging, Helmholtz Zentrum München, Neuherberg, Germany

## \*Correspondence

Vasilis Ntziachristos, Chair of Biological Imaging, Technical University of Munich, Ismaninger Straße 22, D-81675, Munich, Germany.

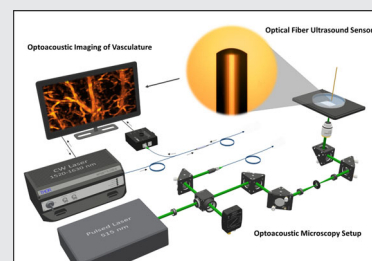
Email: bioimaging.translatum@tum.de

## Funding information

Horizon 2020 Framework Programme, Grant/Award Numbers: MIB 667933, ESOTRAC 732720

## Abstract

Optical fiber sensors can offer robust and miniaturized detection of wideband ultrasound, yielding high sensitivity and immunity to electromagnetic interference. However, the lack of cost-effective manufacturing methods prevents the disseminated use of these sensors in biomedical applications. In this study, we developed and optimized a simple method to create optical cavities with high-quality mirrors for acoustic sensing based on micro-manipulation of UV-curable optical adhesives and electroless chemical silver deposition. This approach enables the manufacturing of ultrasound sensors based on Fabry-Pérot interferometers on optical fiber tips with minimal production costs. Characterization and high-resolution optoacoustic imaging experiments show that the manufacturing process yielded a fiber sensor with a small NEP ( $11 \text{ mPa}/\sqrt{\text{Hz}}$ ) over a broad detection bandwidth (25 MHz), generally outperforming conventional piezoelectric based transducers. We discuss how the new manufacturing process leads to a high-performance acoustic detector that, due to low cost, can be used as a disposable sensor.



## KEYWORDS

endomicroscopy, Fabry-Pérot interferometer, optical fiber sensor, optical resonator, optoacoustic imaging, ultrasound transducer

**Abbreviations:** CW, continuous wave; FBG, fiber Bragg grating; FP, Fabry-Pérot; FPI, Fabry-Pérot interferometry; FWHM, full-width-half-maximum; GRIN, graded index; IR, infra-red; MPE, maximum permissible exposure; ND, neutral density; NEP, noise equivalent pressure; OA, optoacoustic imaging; OR-PAM, optical resolution photoacoustic microscopy; RMS, root mean square; SNR, signal-to-noise ratio.

## 1 | INTRODUCTION

Ultrasound and optoacoustic (OA) sensors commonly comprise piezoelectric transducers with sensitivity proportional to their effective sensing area, hindering their miniaturization [1]. Optical ultrasound sensors have been increasingly implemented as alternatives to piezoelectric transducers in ultrasound and OA imaging systems [2].

This is an open access article under the terms of the Creative Commons Attribution License, which permits use, distribution and reproduction in any medium, provided the original work is properly cited.

© 2021 The Authors. *Journal of Biophotonics* published by Wiley-VCH GmbH.

Among the diverse optical approaches for ultrasound detection [3], sensors based on optical resonators offer attractive features; they are impervious to electromagnetic noise and can be miniaturized without loss of detection sensitivity [4]. Optical fiber sensors in particular are flexible and robust, and are therefore ideal for endomicroscopy applications [5–7]. In parallel, Fabry-Pérot interferometry (FPI)-based optical fiber sensors have gained attention due to their high sensitivity over a broad bandwidth and large acceptance angle. Despite the advantages of these optical fiber sensors, they are difficult to affordably mass produce since the production of optical resonators requires expensive deposition [8] or fiber inscription [9] techniques. Likewise, adjusting the cavity geometry necessitates precise micromanipulation tools. These processes limit the availability of disposable optical fiber ultrasound and OA sensors, and places high durability and sterilization demands on existing sensors for medical applications.

FPI-based optical detection of ultrasound relies on the intensity-modulation of the light reflected from the cavity where acoustic pressure induces optical phase changes. The sensitivity of an FPI-based optical fiber ultrasound sensor can be given as the combination of optical phase sensitivity and acoustic phase sensitivity [10]:

$$S = \frac{dR}{d\phi} \frac{d\phi}{dp} \quad (1)$$

where  $R$  is the light intensity reflected from the fiber,  $\phi$  is the optical phase, and  $p$  is the acoustic pressure incident on the fiber. The first term  $dR/d\phi$  is defined as the optical phase sensitivity, and the second term  $d\phi/dp$  is the acoustic phase sensitivity of the detector. An ideal optical detector should therefore exhibit high finesse and efficient light confinement in the cavity in order to gain optical phase sensitivity [11, 12]. Equally important, the geometry and the material properties like stress-optic coefficients and the Young's modulus should allow good acoustic coupling and strong response to ultrasound, ensuring high acoustic phase sensitivity.

For example, resonators based on  $\pi$ -phase-shifted fiber Bragg gratings ( $\pi$ -FBG) [13] exhibited Q-factors on the order of  $10^5$ , which contributed to a minimum noise equivalent pressure (NEP) of 88 Pa (Table 1). In this design, two Bragg gratings are inscribed in the core of the fiber with a gap, creating an internal sensing cavity. However, the acoustic sensitivity of these sensors is adversely affected by impedance mismatch with external media, leading to the occurrence of strong acoustic reflections at the outer surface of the optical fibers [14]. Additionally, these optical fibers are made of fused silica and experience a small amount of strain per unit pressure due to their inherently large Young's modulus, further diminishing their overall detection performance.

Recent implementations of fiber sensors that feature external sensing cavities close to the acoustic source and low Young's modulus can mitigate limitations stemming from the mechanical properties of fused silica. For example, a fiber sensor with a plano-concave optical microresonator that was built with UV-curable soft polymers and dielectric mirrors has demonstrated higher sensitivity and a NEP value as low as 9.3 Pa at 3.5 MHz over a measurement bandwidth of 20 MHz [15]. In this design, precise polymer vacuum deposition techniques and a strictly defined cavity shape were needed to maintain high back-coupling efficiency to the fiber. Although sensors with such external cavities exhibit high performance, complex tools like vacuum chambers, process monitoring equipment, and precise temperature control systems were required to achieve a high optical sensitivity, which increases manufacturing costs and limits their widespread application. Moreover, the fabrication parameters are predefined, and consequently limit the flexibility for design tuning and optimization to a particular application. Therefore, new low cost, simplified and flexible fabrication methods are required to enable disseminated use of these fiber sensors in OA instrumentation.

In this work, we develop a new sensor design and manufacturing technique to enable the development of inexpensive fiber sensors that could result in disposable units and their widespread integration into clinical

**TABLE 1** Performance parameters of a piezoelectric-based needle hydrophone and several optical fiber ultrasound sensors

	PVDF/PZT	$\pi$ -FBG [13]	$\pi$ -FBG [14]	EFPI [15]	EFPI <sup>a</sup>
Bandwidth (MHz, -3 dB)	25	20	<10	20	25
NEP (Pa)	250	88	450	9.3	54
NEP (mPa/ $\sqrt{\text{Hz}}$ )	50	19.7	142	2.1	11
Sensor area ( $\mu\text{m}^2$ )	$2.0 \times 10^5$	$3.8 \times 10^4$	$3.4 \times 10^4$	$1.2 \times 10^4$	$1.2 \times 10^4$
NEP $\times$ area (mPa. $\mu\text{m}^2/\sqrt{\text{Hz}}$ )	$1.0 \times 10^7$	$7.5 \times 10^5$	$4.8 \times 10^6$	$2.5 \times 10^4$	$1.3 \times 10^5$

Abbreviations: EFPI, extrinsic Fabry-Pérot interferometer; FBG, fiber Bragg grating; PVDF, polyvinylidene fluoride; RI, refractive index.

<sup>a</sup>The fiber sensor developed in this work.

applications. We show that achieving high OA detection performance is possible with simple and robust processes. First, we optimized an electroless chemical silver deposition technique as a cost-effective approach to create high-quality metallic mirrors. Second, we combined this technique with simple micro-manipulation methods of UV-curable optical adhesives to build sensitive cavities on fiber tips.

We demonstrate that the fiber sensors built with our proposed manufacturing methods exhibit a high sensitivity (31 mV/kPa) and small NEP ( $11 \text{ mPa}/\sqrt{\text{Hz}}$ ) over a broad detection band (25 MHz). Moreover, the flexibility of our design enables adjustment and optimization of the detection performance for various applications that require different bandwidth responses. The sensors produced with our method can provide a solution for addressing sterilization requirements in clinical applications where cross-contamination control is essential [16].

## 2 | METHODS

### 2.1 | OA detection principle

The fiber sensor works based on the FPI cavity formed at the tip of single-mode fiber with a cladding diameter of 125  $\mu\text{m}$  and core diameter of 8.5  $\mu\text{m}$  (Figure 1B). The cavity consists of a silver (Ag) mirror at the fiber facet, a plano-concave shaped polymer, and an outer layer of Ag mirror covering the polymer. For ultrasound detection, continuous-wave (CW) infrared laser (IR) beams from a tunable sweep laser source are transmitted into this cavity. The pumping wavelength of the laser is tuned precisely to the sharpest slope of the resonances, ensuring a linear response of the sensor at maximum sensitivity. The superposition of the beams reflecting back from the two mirrors of the resonator is measured simultaneously with a photodiode.

### 2.2 | Manufacturing procedure

In short, the manufacturing procedure is as follows. First, a flat cut at the facet of the fiber (Figure 1C-I) is produced with a cleaving tool (Vytran, Thorlabs, Germany) while ensuring the surface remains free of impurities. Then, a silver mirror is created on the flat facet of the fiber with an electroless wet chemical Ag deposition technique that we optimized specifically to control the reflectivity of the FPI [17]. Our Ag deposition technique allows adjustment of the reflectivity by controlling the reaction speed, deposition time, and concentration of the reactants used. This method allows the mirror reflectivity to be tuned with

high precision to values ranging from 10% to 98%, which is crucial to build FPI cavities with high optical confinement and highest possible optical Q-factor when optical losses within the cavity are inevitable [18].

The Ag deposition procedure starts with forming a complex solution of Ag diamine ( $\text{Ag}[\text{NH}_3]_2\text{NO}_3$ , Tollen's reagent) which contains 5 mL of silver nitrate ( $\text{AgNO}_3$ , 0.1 mol/L, Sigma-Aldrich, Germany), 80  $\mu\text{L}$  of ammonia solution ( $\text{NH}_3$ , 15 mol/L, Sigma-Aldrich) and 200  $\mu\text{L}$  of sodium hydroxide ( $\text{NaOH}$ , 1 mol/L, Carl Roth, Germany) in aqueous form. Then, the cleaved fiber tip is immersed into a 40  $\mu\text{L}$ -drop of the freshly prepared Ag diamine solution (Figure 1C-II) and the chemical reaction is activated by adding a 1:1 ratio of 0.1 mol/L solution of dextrose ( $\text{C}_6\text{H}_{12}\text{O}_6$ ,  $\geq 99.5\%$ , Sigma-Aldrich) as a reducing agent. The reduction-oxidation (redox) process releases elemental silver particles within the solution that come together and construct a thin reflective layer at the fiber facet as they are pulled to the glass surface by adhesion forces. During the chemical reaction, the increase in the intensity of light reflected from the facet is simultaneously measured with a photodiode and monitored with a scope. After the desired reflectivity is achieved, the fiber is removed from the solution. Later, the fiber tip is sonicated with distilled water, and submerged in ethanol to remove residues from the chemical reaction. As a result, a thin (sub-micron) and homogenous Ag layer is formed at the fiber facet.

Following the deposition of the first Ag layer, a plano-concave shaped cap is constructed by dip-coating the fiber with UV curable epoxy (NOA85, Norland). The pre-cured cap thickness was 25  $\mu\text{m}$ ; however due to the UV-curing process, and ambient temperature variations ( $\text{CTE}_{\text{epoxy}} \sim 220 \text{ m}/\text{m}/^\circ\text{C}$ ), the thickness reduced. To achieve high optical back-coupling efficiency and detection bandwidth, we accounted for the post-curing shrinkage in the manufacturing process. For our sensor, an effective thickness of 21  $\mu\text{m}$  was constructed and experimentally confirmed by sweeping the laser frequencies and measuring the free spectral range (FSR) of the resonator. We used the setup shown in Figure 1A for the dip-coating process. When the fiber tip is immersed into a drop of epoxy on a clean glass slide (Figure 1C-III), it collects a certain amount of epoxy that forms the plano-concave shape at the tip upon pulling the fiber back. The viscosity of the epoxy and the speed of immersion and pulling determine the amount of epoxy build-up at the tip. The cavity length and the radius of curvature can be controlled to some extent by adjusting these parameters. For more precise control over the cavity length, we followed the procedure shown in Figure 1D-I-III, which provides an easy and effective solution that requires only manual stages and a microscope slide (Figure 1A). This

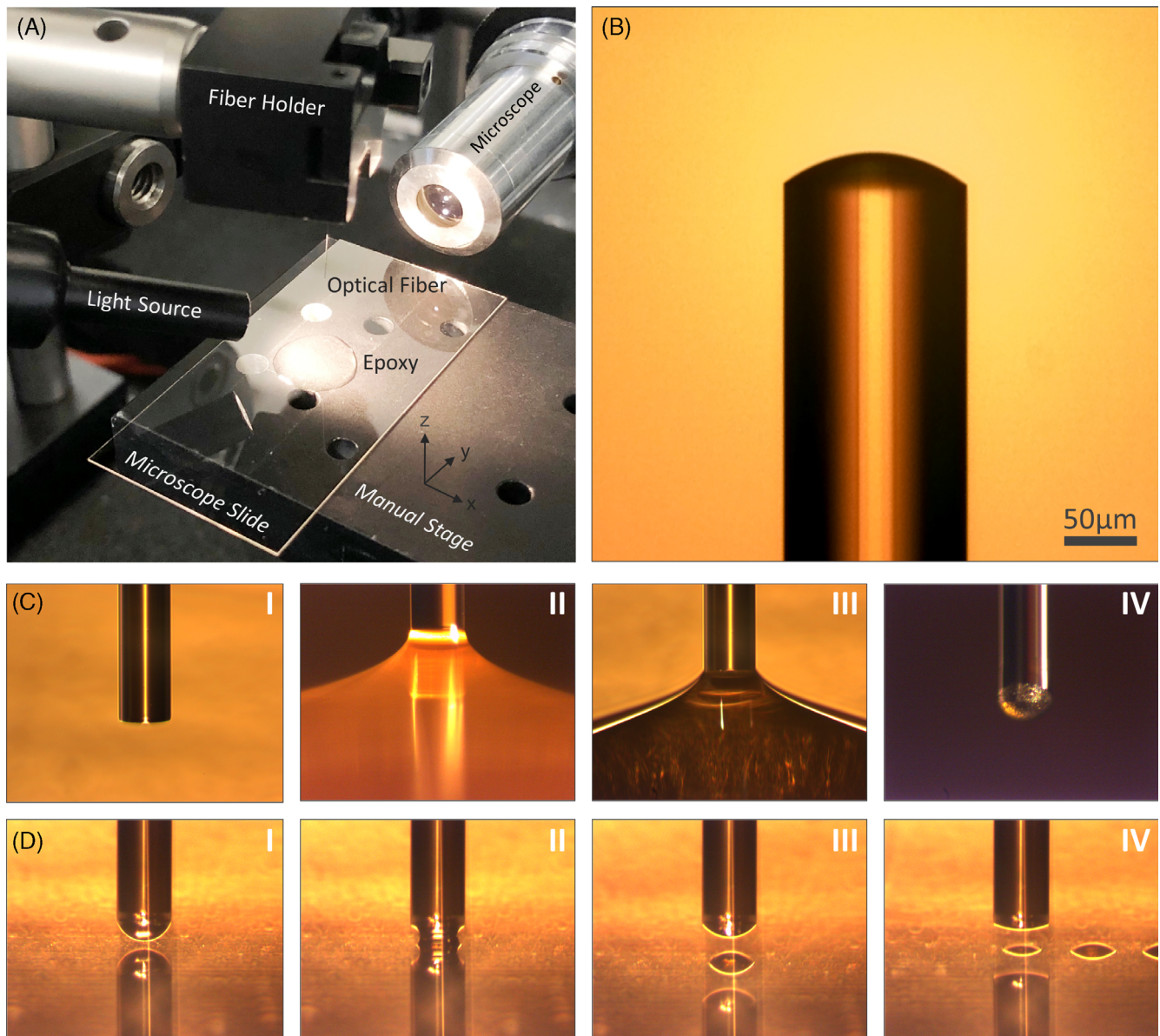


**FIGURE 1** Manufacturing setup and microscopic images from the manufacturing procedure. A, Manufacturing setup used for the epoxy dip coating and the mirror deposition. B, Microscopic image of the fiber sensor after UV-curing process. C, Microscopic images of the fiber during different phases of the manufacturing. I: single-mode optical fiber (125  $\mu\text{m}$ ) after cleaving. II: The optical fiber, immersed in the silver coating solution. The solution, which is half-transparent, becomes darker and more opaque as the chemical reactions develop. III: The optical fiber immersed into UV curable optical adhesive. The adhesive tends to move down slowly toward the fiber facet after the immersion. The amount of adhesive collected around the fiber can be adjusted by controlling the immersion-pulling speed. UV curing of the adhesive follows this step (not depicted). IV: The complete fiber sensor with an ultrasound sensing optical resonator consisting of the silver mirror on the fiber facet, plano-concave polymer, and external silver mirror. D, The procedure for adjusting the cavity length of the sensor by controlling the polymer build-up on the fiber. I: The fiber tip with uncured adhesive positioned above a microscope slide by using manual stages. II: The fiber tip in contact with microscope slide surface. III: The fiber pulled back, leaving a portion of adhesive on the glass surface. IV: Further reduction of the cavity length by repeating the process

simple procedure can be repeated several times (Figure 1D-IV) until reaching the desired amount of epoxy-build, and hence the cavity length. After forming the cavity, the epoxy is cured with UV light from a 14 mW-LED source with a central wavelength of

$\sim 375$  nm. The curing profile of epoxy is adjusted to guarantee its endurance to mechanical impacts while remaining soft and flexible, maximizing mechanical sensitivity to ultrasound waves. The sensing cavity in its final form exhibits high mechanical endurance as a result of

the strong adhesion of the epoxy to metal and fused silica.

Last, the second layer of Ag is deposited on top of the plano-concave shaped epoxy cap following the same methods applied for the first layer of Ag. The fiber is removed from the solution after the reflected light intensity from the cavity reaches its highest level. This procedure results in an Ag mirror with reflectivity exceeding 97% over the interrogation band (1520-1630 nm), as well as at the excitation wavelength (515 nm). The high reflectance of silver at the excitation wavelength prevents pulsed beams back-reflected from the sample from reaching the polymer cavity and minimizes thermally induced noise [19]. The silver coating affords better isolation from external light exposure to the cavity compared to gold, copper, and aluminum, which are also commonly used as coating materials [20]. With the second Ag mirror enclosing the epoxy, the construction of the FPI cavity at the tip of the fiber is completed.

### 2.3 | OA imaging setup

For the characterization and OA imaging experiments, we used an optical resolution photoacoustic microscopy (OR-PAM) setup (Figure 2), which utilizes pulsed laser beams that are excited from a laser source with a wavelength of 515 nm (Flare PQ HP GR 2k-500, Innolight, Germany). The pulse width of the beams from the source is 1.2 ns, and the average repetition rate is 1.2 kHz. Neutral density (ND) filters (Figure 2-NDF) at the laser output were used to lower and adjust the optical power induced on the target. The transmission mode imaging scheme includes a telescopic system and a high-power pinhole (Figure 2B-PH) with an opening diameter of 25  $\mu\text{m}$  (P25C, Thorlabs), spatially cleaning the beam on the optical path. Last, the excitation beam is transmitted in free-space into a 0.25 NA objective lens (PLN 10x, NA 0.25; Olympus, Germany) and focused on the targets to be imaged (Figure 2-OL). In this configuration, the fiber sensor

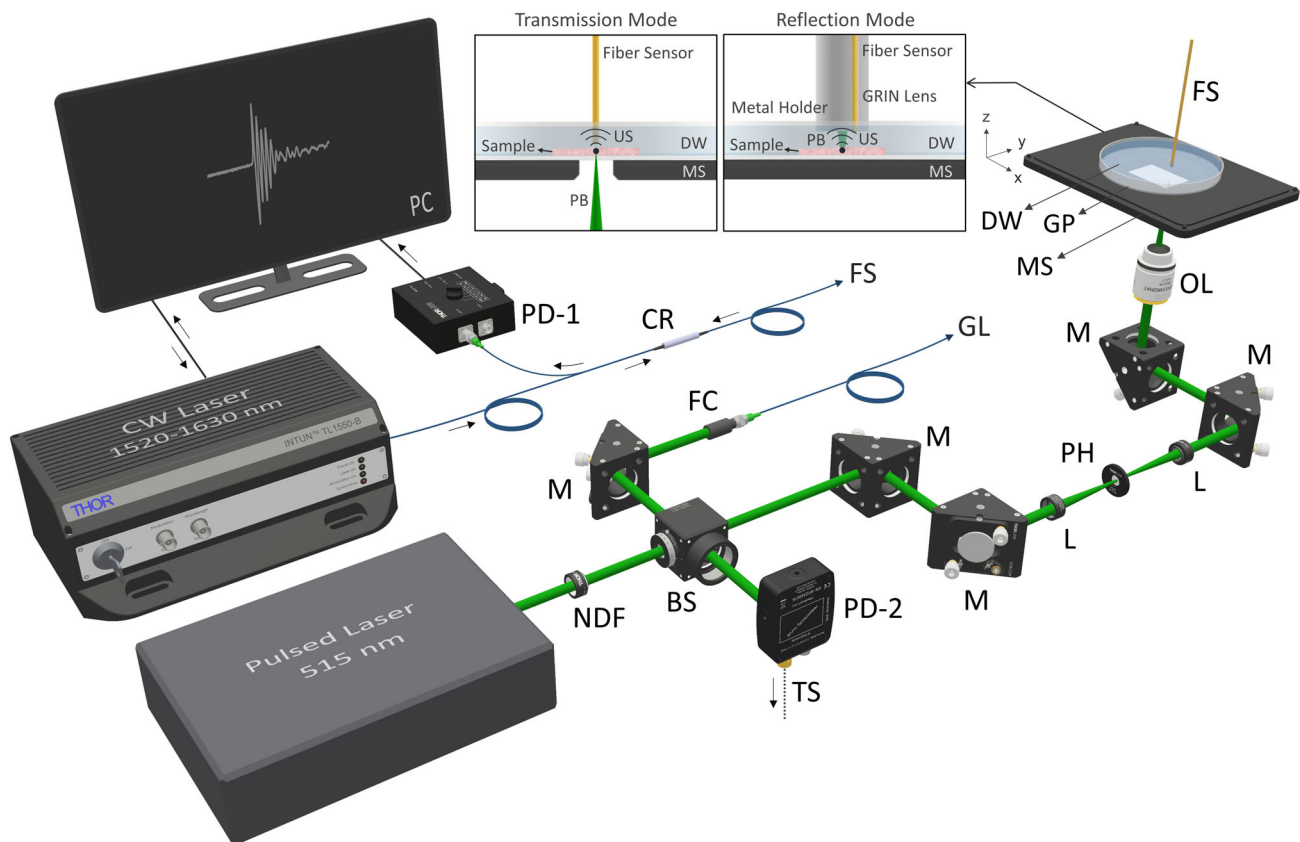


**FIGURE 2** Optoacoustic imaging setup. The optoacoustic excitation, sensor interrogation, and optical resolution photoacoustic microscopy (OR-PAM) imaging setup used for the characterization and experiments are illustrated. The stand-alone fiber labeled with FS positioned above the focal spot of the objective lens shows the configuration in transmission mode imaging. The fiber sensor is positioned on a custom-made holder housing a graded index (GRIN) lens in reflection mode imaging. BS, beam splitter; CR, circulator; DW, distilled water; FS, fiber sensor; GL, GRIN lens; L, lens; GP, glass plate; M, mirror; MS, microscope stage; NDF, neutral density filter; OL, objective lens; PB, pulsed beam; PD, photodiode; PH, pinhole; TS, trigger signal; US, ultrasound

(Figure 2-FS) looks downward to the focal spot while the target is being illuminated from below. For reflection mode (epi-illumination) imaging, the output beam of the ns-laser source was diverted to a separate path and coupled to an optical fiber with a core diameter of 4  $\mu\text{m}$  (Figure 2-FC). This fiber was distally connected to a 2 mm-diameter graded-index (GRIN) lens (Grintech GmbH, Germany). As shown in Figure 2, a custom-made 3D-printed probe was designed to house and position our fiber sensor next to the GRIN lens. The GRIN lens focuses the pulsed laser beams into an optical focal spot with a full-width-half-maximum (FWHM) diameter of 25  $\mu\text{m}$  at the 1.5 mm-working distance of the probe tip. A Si photodiode (DET36A, Thorlabs) (Figure 2-PD-2) placed near the excitation source detects the laser pulses and triggers data acquisition. The optical interrogation source used for acoustic wave detection is a CW tunable laser with a wavelength sweep range of 1520 to 1630 nm and a spectral linewidth of 150 kHz (Intun TLX-1550B, Thorlabs). The fiber-coupled output of this IR laser is transmitted to the sensor through a fiber circulator (CIR1550PM-APC, Thorlabs) (Figure 2-CR). The returning light beam from the sensor goes to an InGaAs photodiode (PDB480C, Thorlabs) (Figure 2-PD-1) via the other channel of the circulator. The optical intensity measured by the photodiode is recorded by using a high-speed 3GS/s data acquisition card (CSE123G2, GaGe; Lockport) and a user interface built on MATLAB software.

### 3 | SENSOR CHARACTERISTICS

#### 3.1 | Sensitivity

We evaluated the NEP of the sensing system as a measure of performance that denotes the lowest detectable and distinguishable level of pressure [21]. This is a practical figure of merit, which takes account of the optical phase sensitivity, acoustic pressure sensitivity, and the noise in the system. NEP is calculated as the ratio between the root-mean-square (RMS) noise induced on the detection system and the sensitivity of the ultrasound sensor over its detection bandwidth. In characterization experiments, we used a 0.5 mm-diameter calibrated needle hydrophone (Precision Acoustics, United Kingdom) with an average sensitivity of 438.5 mV/MPa for a frequency band of 5 to 30 MHz. A focused pulsed laser beam was delivered to 125  $\mu\text{m}$ -thick black vinyl tape (Type 764, 3M, Germany), which shows surface uniformity and homogenous absorption. Distilled water was used as the acoustic coupling medium in this experimental setup. During the measurements with the fiber sensor, precise wavelength tuning of the interrogation laser to the sharpest slope of the resonance notches shown in

Figure 3A provided the highest sensitivity. The fiber sensor exhibits a phase response with a maximum non-linearity <3% over a dynamic range as large as 3.72 V. Figure 3B gives a comparison of temporal responses measured with the fiber sensor and a calibrated needle hydrophone in these measurements. The signal acquired with the needle hydrophone was scaled up 20 times for better visibility in the figure. By normalizing the peak-to-peak voltage amplitude measured with the needle hydrophone, the exact value of pressure at a certain distance from the source was determined; the sensitivity of the fiber sensor was found to be 31 mV/kPa over a 25 MHz bandwidth. This value corresponds to an upper limit of linear detection of 120 kPa, which is sufficiently above the typical peak pressure amplitudes generated for in vivo OA imaging (<20 kPa) [22].

The sensitivity characterization experiments show that the developed fiber sensor provides 70-fold higher sensitivity than the calibrated needle hydrophone. The fiber sensor exhibits high detection performance despite its small size as a result of the external micro resonator made of soft epoxy enabling efficient overlay of strong optical energy with ultrasound waves. In contrast, the sensitivity of the conventional piezoelectric-based transducer in the needle hydrophone depends strictly on its large detection area. Comparing the acoustic sensitivity per area of the two sensors reveals the superiority of the fiber sensor, which is more than three orders of magnitude more sensitive per unit area than the needle hydrophone. Despite a relatively higher RMS noise level in the fiber sensor interrogation setup, our sensor provides substantially higher sensitivity and signal-to-noise ratio (SNR) over the needle hydrophone (Figure 3B). The NEP of the OA imaging setup with the fiber sensor was measured as 54 Pa (11 mPa per  $\sqrt{\text{Hz}}$ ), which is five times better than the NEP of the needle hydrophone.

The detection sensitivity of the developed FPI-based resonator is predominantly determined by the change in the physical cavity length ( $l_c$ ) [23]. In addition, the cavity of our sensor is comprised of soft epoxy having extremely low stress-optic coefficients [24, 25]. Therefore, contributions from the elasto-optic effect are negligible. The acoustic phase sensitivity ( $S_\phi$ ) of our sensor can be expressed as:

$$S_\phi = \frac{d\phi}{dp} = -\frac{4\pi n l_c}{\lambda_{\text{res}}} \left( \frac{1}{\lambda_{\text{res}}} \frac{d\lambda_{\text{res}}}{dp} \right) \quad (2)$$

where  $n$  is the refractive index,  $l_c$  is the cavity length,  $\lambda_{\text{res}}$  is the resonance wavelength. The second term is the normalized sensitivity ( $S_\lambda$ ), which is defined as the normalized shift of the resonance wavelength ( $d\lambda_{\text{res}}/\lambda_{\text{res}}$ ) per unit pressure ( $dp$ ). From Figure 3A, we find that the resonance at around 1572 nm has a slope of 1763 mV/nm

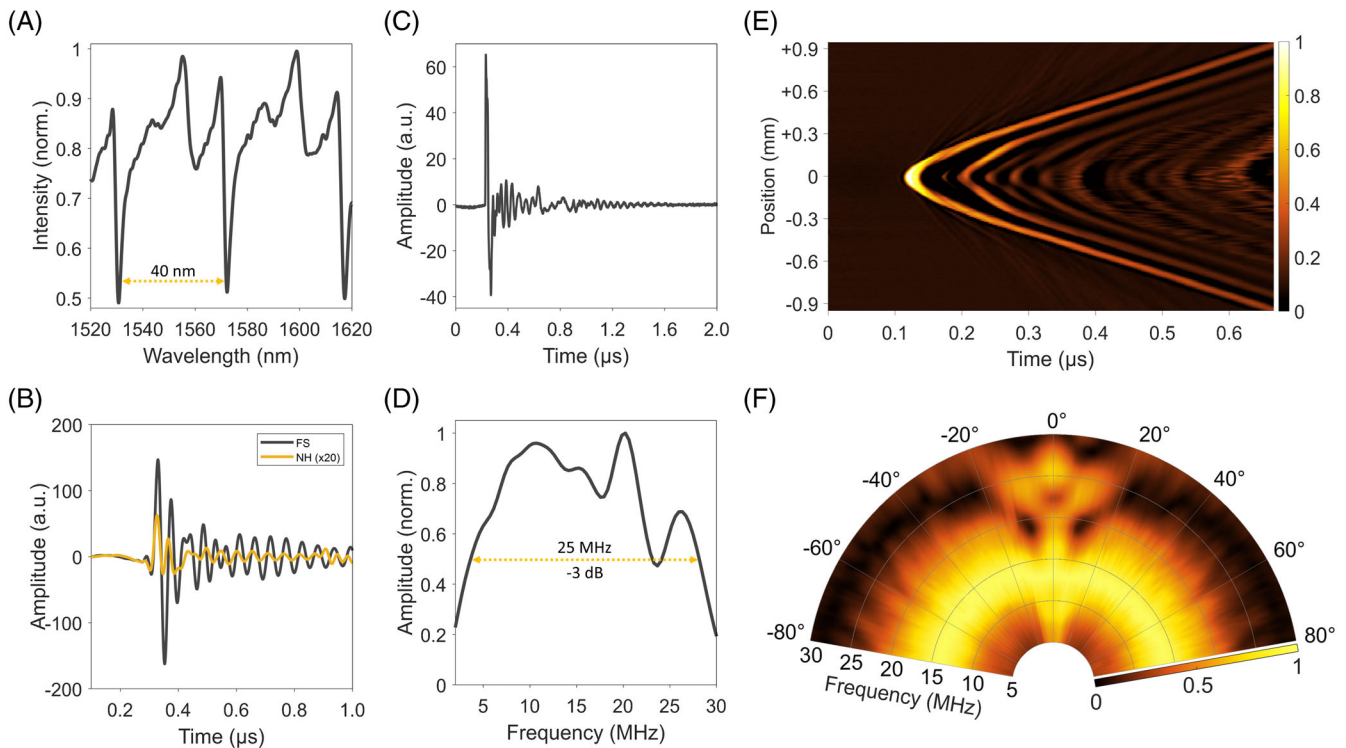


**FIGURE 3** Fiber sensor characteristics and performance. A, The reflection spectrum of the fiber sensor. The free spectral range (FSR) was measured as 40 nm, which corresponds to a cavity length of 21  $\mu\text{m}$  ( $\text{FSR} = \lambda_0^2/2nL_c$ ). B, Temporal responses measured with the fiber sensor (FS) and a calibrated needle hydrophone (NH) above a point ultrasound source on 125  $\mu\text{m}$ -thick black tape. The yellow line shows the signal acquired with the calibrated needle hydrophone and scaled up 20 times for better visibility, while the black line shows the signal acquired with the fiber sensor without scaling. The acoustic responsivity of the fiber sensor is 70-fold higher than that of the needle hydrophone when comparing the peak-to-peak amplitudes of the signal. C, The temporal response of the fiber sensor measured above a point optoacoustic source from a thin gold layer sputtered on a microscope glass slide. D, Acoustic frequency response of the fiber sensor. E, The spatial response of the fiber sensor based on a time-resolved optoacoustic signal, which was acquired by a line scan over an ultra-wide bandwidth ultrasound point source. F, Acoustic frequency spatial response of the fiber sensor, showing frequency response with respect to the angle of incidence of acoustic waves to the fiber. The tip of the sensor was positioned  $\sim 160 \mu\text{m}$  above the imaging plane, and the angle of incidence of ultrasound waves to the fiber sensor tip was within the range of  $\pm 80^\circ$

over a dynamic range of 3.72 V. Based on this value and the measured sensitivity of the sensor, the normalized sensitivity ( $S_\lambda$ ) of our sensor is found to be  $0.0112 \text{ MPa}^{-1}$ . This fractional wavelength shift per unit pressure has been reported to be  $\sim 2.5 \times 10^{-6} \text{ MPa}^{-1}$  for FBG inscribed silica fibers [26], and  $\sim 21 \times 10^{-6} \text{ MPa}^{-1}$  for silicon waveguides spin-coated with BCB polymer [27], highlighting the advantage of our approach, which does not require such complex manufacturing methods.

### 3.2 | Frequency response

Frequency response characterization of the fiber sensor was done based on an analysis of measured acoustic signals from an ultra-wide bandwidth ultrasound point source. This point source was generated by focusing a pulsed laser beam (wavelength: 515 nm, pulse width:

1.2 ns) onto a gold (Au) layer with a uniform thickness of 200 nm, which was sputtered onto a glass slide [28]. Figure 3C shows the temporal response of the fiber sensor. The measured signals were filtered with a 2 to 500 MHz band-pass filter and averaged  $1 \times 10^3$  times for denoising. As shown in Figure 3D, the manufactured fiber sensor exhibits a wide bandwidth over 25 MHz with  $-6 \text{ dB}$  cut-off frequency at 29.6 MHz. Figure 3E shows a line scan (B-scan) over the same wideband acoustic point source that was used to estimate the spatial responsivity and directivity characteristics of the fiber sensor over angles of incidence of  $\pm 80^\circ$  [29]. The time-resolved OA signals were Fourier transformed and normalized at each position along the path of the scan. As observed in Figure 3F, the fiber sensor exhibits less directivity and high acoustic detection sensitivity over its bandwidth and an isotropic response at frequencies up to 25 MHz.

## 4 | IMAGING EXPERIMENTS

The imaging performance of the fiber sensor was tested in both transmission and reflection mode using OR-PAM setups with the sensor oriented for forward-looking detection, reflecting its likely configuration in potential clinical applications. In transmission mode, the stand-alone fiber sensor (Figure 2-FS) was positioned 250  $\mu\text{m}$  above a focused laser beam with a FWHM diameter of 10  $\mu\text{m}$  (Figure 2-PB). The excitation wavelength was 515 nm, and the average optical power at the microscope objective output was measured to be 290  $\mu\text{W}$ . In the reflection mode OR-PAM setup, the fiber sensor was embedded in a custom-made imaging probe, which also housed a GRIN lens (Grintech GmbH) (Figure 2-FS-GL).

The output beam from the GRIN lens had a FWHM diameter spot size of 25  $\mu\text{m}$  at the 1.5 mm-working distance of the probe tip. The distal ends of the fiber sensor and the GRIN lens were positioned at the same distance from the imaging plane in order to mimic realistic endoscopic imaging conditions. The average output power was 450  $\mu\text{W}$ , as measured before and after imaging experiments. The peak fluence at the focal spot was close to the maximum permissible exposure (MPE) for human skin (20  $\text{mJ}/\text{cm}^2$ ) [30]. We did not observe any optical damage to the phantoms.

Figure 4 shows the resulting maximum intensity projection-based OA images of suture phantoms and tissue samples acquired by scanning the selected regions-of-interest with a translational microscope stage and

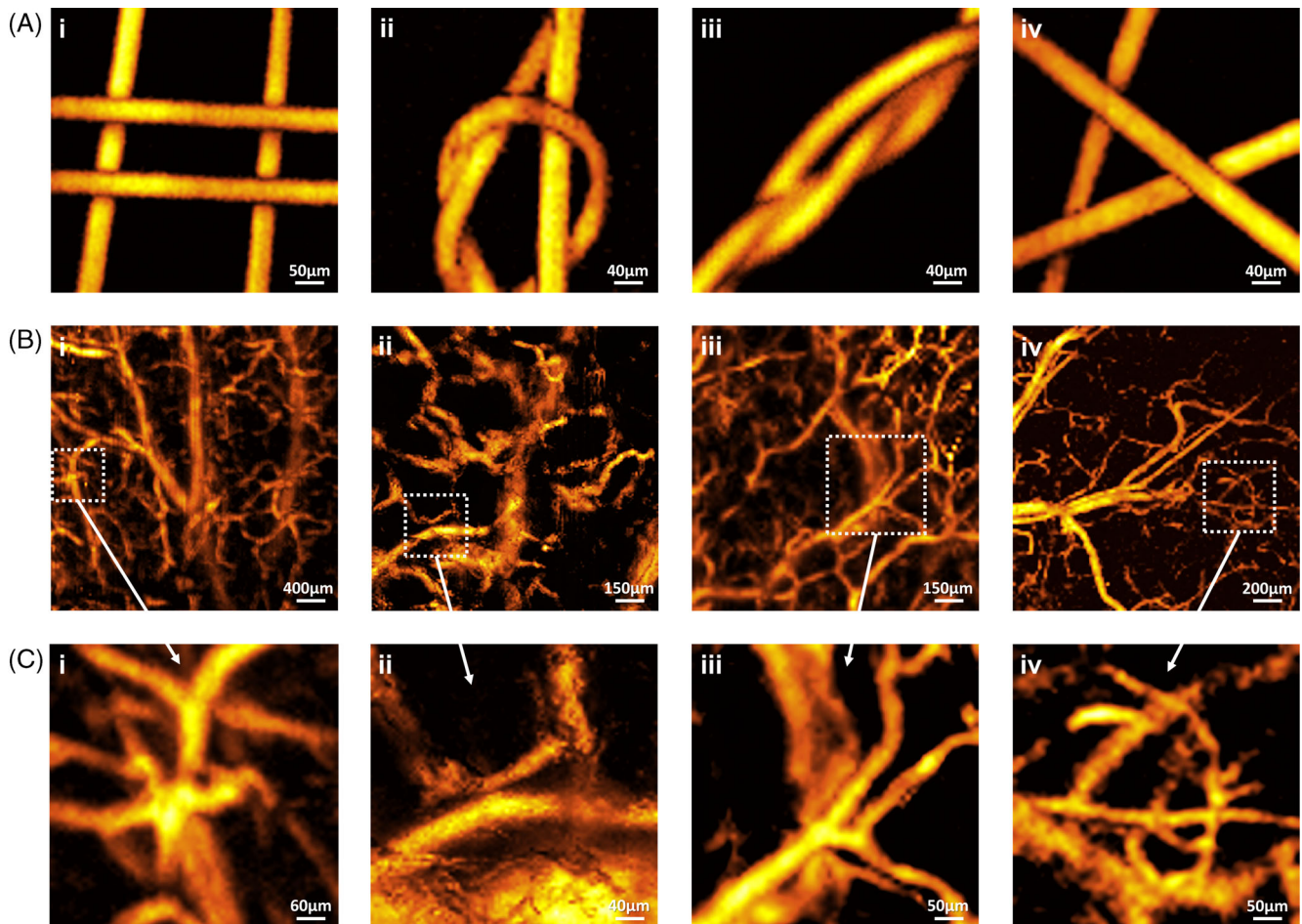


**FIGURE 4** Optical resolution photoacoustic microscopy (OR-PAM) images of phantoms and ex vivo mouse ear. The field of view of each image is 10 times the scale bar indicated on the bottom-right corner. Regions framed with dashed white boxes were imaged separately with smaller step sizes and are shown in corresponding sub-figures. In transmission mode, the stand-alone fiber sensor was placed on top of the samples while it was being illuminated with a focused beam coming from an objective lens. In reflection mode, the fiber sensor was placed next to a graded index (GRIN) lens on a custom-made probe for reflection mode imaging. A, Reflection mode OR-PAM images of phantoms prepared with 30  $\mu\text{m}$  thick black polyamide medical-grade sutures. B, OR-PAM images of ex-vivo mouse ears with raster scanning step size of 10  $\mu\text{m}$  in transmission mode (i-iii), and 20  $\mu\text{m}$  in reflection mode (iv). C, Images of the regions of interests within the corresponding dashed boxes acquired with a raster scanning step size of 5  $\mu\text{m}$

resolved with high SNR provided by the fiber sensor. Figure 4A shows the reflection mode images of knots made with 30  $\mu\text{m}$ -thick black polyamide medical-grade sutures (Vetsuture, France), mimicking microvascular structures in biological tissue. Figure 4B,C show the vascular structures within the regions of interest on ex-vivo mouse ears (i-iii: transmission mode; iv: reflection mode). The regions within the dashed boxes in Figure 4B were scanned with higher scanning precision to reveal more details and are shown in corresponding sub-figures (Figure 4C). The magnified insets in Figure 4C depict micro capillaries on the order of 20  $\mu\text{m}$ . For all images, the signals acquired with the fiber sensor at each position were averaged 50 times and passed through a band-pass filter of [5-100] MHz.

## 5 | DISCUSSION

The widespread dissemination of high-resolution OA imaging requires miniaturized ultrasound sensors with high responsivity throughout a large bandwidth [31], which can also be economically produced. To this end, we developed a simple manufacturing procedure and realized an optical fiber sensor that provides excellent ultrasound detection performance together with practical advantages, such as a small footprint, robustness, and flexibility. The “in-house” manufactured sensor featuring a fiber-based external optical resonator exhibits highly sensitive wideband ultrasound detection (11 mPa/ $\sqrt{\text{Hz}}$ ). In addition to outperforming conventional piezoelectric transducers, the developed sensor provides a cost-effective solution for high resolution and high fidelity OA imaging, which makes it advantageous over several other implementations of optical ultrasound sensors (Table 1).

Our fiber sensor utilizes an external sensing cavity that is made of epoxy ( $Z_{\text{epoxy}} \sim 2 \times 10^6 \text{ kg/m}^2\text{s}$ ), providing acoustic impedance matching with the surrounding medium ( $Z_{\text{water}} \sim 1.48 \times 10^6 \text{ kg/m}^2\text{s}$ ) and minimizing losses from acoustic reflections [32, 33], which is especially important for retaining a uniform high detection sensitivity at high frequencies [34]. Because the epoxy has a low Young's modulus, it experiences a strong strain per unit pressure. The induced strain is further enhanced by backing the sensing cavity with rigid silica glass ( $Z_{\text{silica}} \sim 13.1 \times 10^6 \text{ kg/m}^2\text{s}$ ). Our fiber sensor's rigid-backing design results in a flatter frequency response over a sufficiently wide bandwidth and a sensitivity double than that of matched-load configurations [35]. The detection bandwidth of our sensor (25 MHz) is mainly determined by the spatial distribution of ultrasound waves along the optical propagation axis in the FPI cavity. Therefore, the detection bandwidth is inversely proportional to the

cavity length when acoustic attenuation and scattering in the cavity medium are assumed to be negligible ( $f_{\text{cutoff}} = v_0/2l_c$ ) [32].

The electroless chemical deposition method that we optimized for sensor manufacturing provides a feasible solution to produce silver mirrors with reflectivity values similar to that of dielectric mirrors. Our silver deposition method also enables the creation of an external submicrometer-thin coating that is transparent to high-frequency ultrasound waves, incident on the sensor. In contrast, hard dielectric mirrors with larger thicknesses ( $\sim 3 \mu\text{m}$ ) would cause acoustic impedance mismatches with the external medium, and therefore adversely affect the propagation of ultrasound and the frequency response of the sensor [36]. In the future, we plan to further refine our chemical deposition process and reduce optical absorption and scattering of the silver mirrors with supplemental post-treatments, which would yield a higher optical phase sensitivity.

Although we demonstrated a single fiber sensor in this work, our sensor design and scalable, low-cost manufacturing procedure affords both reproducibility and high flexibility to control sensor characteristics and performance. The cavity length and the bandwidth of the sensor can be set precisely by modifying the amount of epoxy build-up at the fiber tip. The electroless chemical silver deposition method allows optimization of the reflectivity of the mirrors during the manufacturing procedure. Future efforts will focus on manufacturing fiber sensors with different bandwidth responses customized for specific applications and demonstrating the advantages of our approach for in vivo OA endomicroscopy. In addition, single-frequency light sources with narrow linewidth could be implemented to perform optical-based acoustic sensing [37], leading to phase noise reduction and increased detection sensitivity of the system.

## 6 | CONCLUSION

The developed fiber sensor is a practical solution for diverse imaging applications due to its high detection performance and flexible design, which allows for precise adjustment of the bandwidth. Furthermore, our optimized fiber ultrasound sensor manufacturing approach can easily be translated to mass-production, paving the way to make such sensors readily available for clinical endomicroscopy applications. Low-cost production and disposability of the sensor can potentially address cross-contamination control requirements without the need for disinfection and sterilization after each measurement, which is problematic for most probes.

## ACKNOWLEDGMENTS

This project has received funding from the European Union's Horizon 2020 research and innovation programme under grant agreement no. 667933 (MIB) and C.Z. additionally under grant agreement 732720 (ESOTRAC). The authors wish to acknowledge Dr. J. P. Fuenzalida Werner for useful discussions and Dr. Robert J. Wilson for assistance in editing the manuscript. Open access funding enabled and organized by Projekt DEAL.

## DATA AVAILABILITY STATEMENT

The data that support the findings of this study are available from the corresponding author upon reasonable request.

## ORCID

Okan Ülgen  <https://orcid.org/0000-0002-1414-844X>

## REFERENCES

- [1] A. Taruttis, V. Ntziachristos, *Nat. Photonics* **2015**, 9, 219.
- [2] G. Wissmeyer, M. A. Pleitez, A. Rosenthal, V. Ntziachristos, *Light Sci. Appl.* **2018**, 7, 53.
- [3] B. Dong, C. Sun, H. F. Zhang, *IEEE Trans. Biomed. Eng.* **2017**, 64, 4.
- [4] R. Shnaiderman, G. Wissmeyer, O. Ülgen, Q. Mustafa, A. Chmyrov, V. Ntziachristos, *Nature* **2020**, 585, 372.
- [5] Y. Wang, H. Yuan, X. Liu, Q. Bai, H. Zhang, Y. Gao, B. Jin, *IEEE Access.* **2019**, 7, 85821.
- [6] R. Ansari, E. Z. Zhang, A. E. Desjardins, P. C. Beard, *Light Sci. Appl.* **2018**, 7, 75.
- [7] G. Wissmeyer, D. Soliman, R. Shnaiderman, A. Rosenthal, V. Ntziachristos, *Opt. Lett.* **2016**, 41, 1953.
- [8] D. M. Mattox, *Handbook of Physical Vapor Deposition (PVD) Processing*, 2nd ed., Elsevier, Burlington, MA, USA, **2010**, p. 218.
- [9] R. Kashyap, *Fiber Bragg Gratings*, 2nd ed., Elsevier, Burlington, MA, USA, **2009**, p. 53.
- [10] P. Morris, A. Hurrell, A. Shaw, E. Zhang, P. Beard, *J. Acoust. Soc. Am.* **2009**, 125, 3611.
- [11] S. Ashkenazi, H. Yang, S. W. Huang, in *Photoacoustic Imaging and Spectroscopy* (Ed: L. V. Wang), CRC Press, Boca Raton, FL, USA, **2017**, p. 223.
- [12] J. Li, A. Taylor, I. Papakonstantinou, E. Zhang, P. C. Beard, Proc. SPIE 8943, Photons Plus Ultrasound: Imaging and Sensing, March 2014.
- [13] R. Shnaiderman, G. Wissmeyer, M. Seeger, D. Soliman, H. Estrada, D. Razansky, A. Rosenthal, V. Ntziachristos, *Optica* **2017**, 4, 1180.
- [14] A. Rosenthal, D. Razansky, V. Ntziachristos, *Opt. Lett.* **2011**, 36, 1833.
- [15] J. A. Guggenheim, J. Li, T. J. Allen, R. J. Colchester, S. Noimark, O. Ogunlade, I. P. Parkin, I. Papakonstantinou, A. E. Desjardins, E. Z. Zhang, P. C. Beard, *Nat. Photonics* **2017**, 11, 714.
- [16] H. Su, I. I. Iordachita, J. Tokuda, N. Hata, X. Liu, R. Seifabadi, S. Xu, B. Wood, G. S. Fischer, *IEEE Sens. J.* **2017**, 17, 1952.
- [17] M. Schlesinger, *Modern Electroplating*, 5th ed., John Wiley & Sons, Inc., Hoboken, NJ, USA, **2010**, p. 131.
- [18] H. Varu, *Ph.D. Thesis*, University College London **2014**.
- [19] S. Babar, J. H. Weaver, *Appl. Optics* **2015**, 54, 477.
- [20] K. M. McPeak, S. V. Jayanti, S. J. P. Kress, S. Meyer, S. Iotti, A. Rossinelli, D. J. Norris, *ACS Photonics* **2015**, 2, 326.
- [21] L. V. Wang, L. Gao, *Annu. Rev. Biomed. Eng.* **2014**, 16, 155.
- [22] E. Zhang, J. Laufer, P. Beard, *Appl. Optics* **2008**, 47, 561.
- [23] B. T. Cox, P. C. Beard, *IEEE Trans. Ultrason. Ferroelectr. Freq. Control* **2007**, 54, 394.
- [24] T. A. Pittsa, J. F. Greenleaf, *J. Acoust. Soc. Am.* **2000**, 108, 2873.
- [25] F. Hossain, H. P. Chan, M. A. Uddin, *Appl. Optics* **2010**, 49, 403.
- [26] C. A. F. Marques, D. J. Webb, P. Andre, *Opt. Fiber Technol.* **2017**, 36, 144.
- [27] R. R. Kumar, E. Hahamovich, S. Tsesses, Y. Hazan, A. Grinberg, A. Rosenthal, *IEEE Photonics J.* **2019**, 11, 3.
- [28] E. M. Strohm, E. S. L. Berndl, M. C. Kolios, *Photoacoustics* **2013**, 1, 49.
- [29] H. Li, B. Dong, Z. Zhang, H. F. Zhang, C. Sun, *Sci. Rep.* **2014**, 4, 4496.
- [30] L.I. of America, American National Standard for Safe Use of Lasers, ANSI Z136.1-2000, **2007**.
- [31] S. Jeon, J. Kim, D. Lee, J. W. Baik, C. Kim, *Photoacoustics* **2019**, 15, 100141.
- [32] P. C. Beard, F. Pérennés, T. N. Mills, *IEEE Trans. Ultrason. Ferroelectr. Freq. Control* **1999**, 46, 1575.
- [33] L. E. Kinsler, A. R. Frey, A. B. Coppens, J. V. Sander, *Fundamental Acoustics*, John Wiley & Sons Inc, Hoboken, NJ, USA, **2001**, p. 435.
- [34] X. L. Den-Ben, D. Razansky, V. Ntziachristos, *Phys. Med. Biol.* **2011**, 56, 6129.
- [35] P. C. Beard, T. N. Mills, *Appl. Optics* **1996**, 35, 663.
- [36] J. Buchmann, J. Guggenheim, E. Zhang, C. Scharfenorth, B. Spannekrebs, C. Villringer, J. Laufer, *Appl. Optics* **2017**, 56, 17.
- [37] H. N. Kenhagho, F. Canbaz, R. Guzman, P. Cattin, A. Zam, *Sens. Actuator A Phys.* **2021**, 317, 112394.

**How to cite this article:** Ülgen O, Shnaiderman R, Zakian C, Ntziachristos V. Interferometric optical fiber sensor for optoacoustic endomicroscopy. *J. Biophotonics*. 2021;14:e202000501. <https://doi.org/10.1002/jbio.202000501>